Structure, Stoichiometry, and Phase Purity of Calcium Substituted Lanthanum Manganite Powders

S. Faaland,* K. D. Knudsen,† M.-A. Einarsrud,* L. Rørmark,* R. Høier,‡ and T. Grande*,[1]

*Department of Inorganic Chemistry, and ‡Department of Physics, Norwegian University of Science and Technology, 7034 Trondheim, Norway; and
†SNBL, ESRF, BP 220, 38043 Grenoble Cedex, France
E-mail: Tor.Grande@chembio.ntnu.no

Calcium-doped lanthanum manganite $La_{1-x}Ca_xMnO_3$, synthesized by the glycine/nitrate method, was characterized by high resolution synchrotron X-ray powder diffraction, electron diffraction, and infrared spectroscopy. A strong correlation was observed between the cooling rate from the calcination temperature and the powder quality, indicating the importance of a homogeneous oxygen stoichiometry. The structure refinement reveals that $La_{1-x}Ca_xMnO_3$ with $x = 0.2, 0.3, 0.4$, and 0.6 has orthorhombic symmetry with space group *Pnma*. The MnO_6 octahedra are fairly symmetrical, but the octahedra are tilted about 20° relative to the ideal perovskite structure. Infrared spectroscopy revealed that only the O–Mn–O bending mode is significantly influenced by the substitution of La with Ca. In $La_{0.8}Ca_{0.2}MnO_3$ we found diffraction evidence of a superstructure in domains in some of the grains. We propose that the superstructure in $La_{0.8}Ca_{0.2}MnO_3$ is due to ordering of Ca^{2+} ions on A (La^{3+}) sites in the perovskite ABO_3 structure. © 1998 Academic Press

1. INTRODUCTION

Calcium-substituted lanthanum manganite, $La_{1-x}Ca_x MnO_3$ (LCM), is a promising material for high temperature solid oxide fuel cell (SOFC) cathodes because of its high electrical conductivity and good compatibility with cubic stabilized zirconia (1). The cathodes are prepared by sintering of powders, whose characteristics highly influence properties as electron and ion transport parameters, oxygen permeability, porosity, solid-electrolyte interaction, etc., of the finally obtained ceramic. The detection of magnetoresistive properties in manganates has stimulated the interest in calcium substituted lanthanum manganates (2). LCM exhibits extremely large changes in electrical resistance in response to applied magnetic fields, a property that is of technological relevance for the development of magnetic memory and switching devices. These applications of LCM

powders are dependent on the structure, stoichiometry, and phase purity.

Over the last three years there have been various suggestions regarding the symmetry of the LCM compounds. Shuk *et al.* (3) and Mahendrian *et al.* (4) both determined $La_{1-x}Ca_xMnO_3$ to be rhombohedral for $x < 0.2$ and cubic for $x \geq 0.2$. However, a recent study by Radaelli *et al.* (5) on $La_{1-x}Ca_xMnO_3$ with two other doping levels ($x = 0.25$ and 0.5) shows that the structure is orthorhombic with space group *Pnma*. In the present work we report on the structure of $La_{1-x}Ca_xMnO_3$ ($x = 0.2, 0.3, 0.4, 0.6$) studied by synchrotron X-ray powder diffraction, electron diffraction, and IR spectroscopy, and find orthorhombic symmetry.

2. EXPERIMENTAL PROCEDURE

2.1. Synthesis

LCM powders containing 20, 30, 40, and 60 mol% of calcium on the La site were prepared by means of the glycine/nitrate method (6). This method ensures a uniform composition of the crystallites and produces a single phase, submicron powder with high surface area. The glycine and the nitrates were supplied by Merck and had a purity of 98.5%. A molar ratio of 0.65 between glycine and nitrate was found appropriate for producing single phase perovskite compounds except for the sample containing 60 mol% of Ca on the La site where a molar ratio of 0.55 was used. The raw powders were ball-milled in ethanol for 5 h before calcination. The powders were then calcined in air according to the program shown in Fig. 1. After heat treatment at 1000°C for 120 h, the powder was cooled to 800°C at 5°C/h and subsequently from 800 to 500°C at 2°C/h to ensure a homogeneous oxygen stoichiometry. The powders we first prepared were cooled by a rate of 25°C/h from the calcination temperature. Later the temperature profile shown in Fig. 1 was used for calcination. These powders were labeled "slow" cooled, while the powders annealed in the first mentioned way were labeled "fast" cooled. After the calcination,
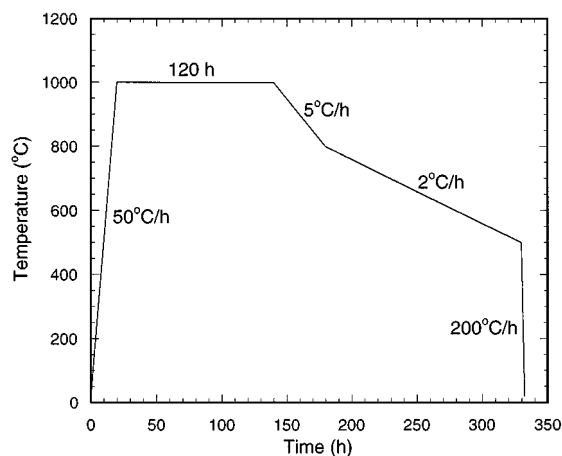
FIG. 1. Calcination program for the LCM powders.

the powders were again ball-milled in ethanol to break down agglomerates to obtain submicron powders.

2.2. Characterization

Chemical analysis of the cations was performed by inductively coupled plasma atomic emission spectroscopy using an Atom Scan 16-ICP-AES spectrometer (Thermo Jarrell Ash Corp., USA). The standard deviations in the measurements were less than 1%. The oxygen concentration was determined by iodometric titration (7). The maximum standard deviation was 0.5%.

The structure determinations were made on the "slow" cooled compounds. X-ray powder diffraction data were collected on the Swiss–Norwegian beamline (SNBL) at the European Synchrotron Research Facility (ESRF) in Grenoble, France, using a wavelength of 0.8022 Å. In order to determine the space group symmetry, extended regions of the powder pattern ($1 < 2\theta < 80°$) were collected for all the samples. A Si 111 analyzer crystal was employed in the diffracted beam, giving an instrumental resolution of $0.012°$ $-0.020°$ over this 2θ range. A high resolution was crucial to be able to index the line-splittings in the LCM compounds, and from the obtained patterns we were able to find the cell symmetry and structural parameters. The position of a certain number of peaks (20 to 40 depending on the LCM composition) were extracted from the pattern by means of the program PEAKFIND (8) and a first approximation to the lattice parameters was found by using the autoindexing program ITO (9). Extraction of intensities from the powder pattern was done by means of the program PROFIL (10), which performs a Le Bail deconvolution to distribute the intensities. A pseudo-Voigt peak shape function was assumed. Finally, the structure was refined using the PC version of the program package GSAS (11).

The consistency and reproducibility of the results was checked by comparing them with those obtained by the Rietveld analysis program WIN-RIETVELD from Siemens under the same strategy, including the refinement of (i) background parameters, (ii) scale factors, (iii) instrumental effects (zero-point 2θ shift and systematic shifts, depending on absorption and sample off-centering), (iv) structural parameters (lattice parameters and fractional coordinates of the cations), and (v) profile parameters (half-width parameters and the mixing parameter of the pseudo-Voigt function).

Selected area electron diffraction (SAED) and convergent beam electron diffraction (CBED) were performed to determine point-group symmetry using a Phillips CM30 (300 kV) transmission electron microscope (TEM). Samples for TEM analysis were prepared by grinding the fine powder under ethanol and keeping the suspension in an ultrasonic bath for 20 min, after which a drop of suspension was spread onto a TEM copper grid covered by a holey carbon film.

Further structure characterization was performed by infrared (IR) spectroscopy (Bruker IFS 66v) using 1 wt% LCM in polyethylene pellets.

The size and shape of the powder crystallites were investigated by scanning electron microscopy (SEM) (Zeiss DSM 940). The specific surface area was found by using the BET isotherm from nitrogen absorption (Micromeritics ASAP 2000).

3. RESULTS AND DISCUSSION

The morphology of the powders before and after calcination is shown in Fig. 2. The raw powders show extensive particle agglomeration, a result of the synthesis method. The high temperatures occuring during the synthesis process cause the particles to be partially sintered (i.e. necked together), resulting in the formation of significantly larger agglomerated secondary particles having an open, high surface area structure (12). Typically, the precalcined powders have a bimodal distribution with some small, 1–5 μm, agglomerates, but with most of the powder consisting of 10–50 μm agglomerates. After ball-milling, calcination, and further ball-milling the agglomerates are broken down and the particles are rounded and submicron (0.1–0.5 μm) as shown in Fig. 2b. The BET specific area is about 5.5 m^2/g for all substitution degrees, which is consistent with an average particle diameter of 0.2 μm assuming spherical particles.

The chemical composition of the calcined powders are listed in Table 1. The $La_{1-x}Ca_xMnO_3$ samples with $x = 0.2$ and 0.3 are cation deficient, while the samples with $x = 0.4$ and 0.6 are anion deficient relative to the ideal perovskite stoichiometry.

According to the X-ray diffraction patterns all powders are single phase perovskite-type oxides. Extraneous lines
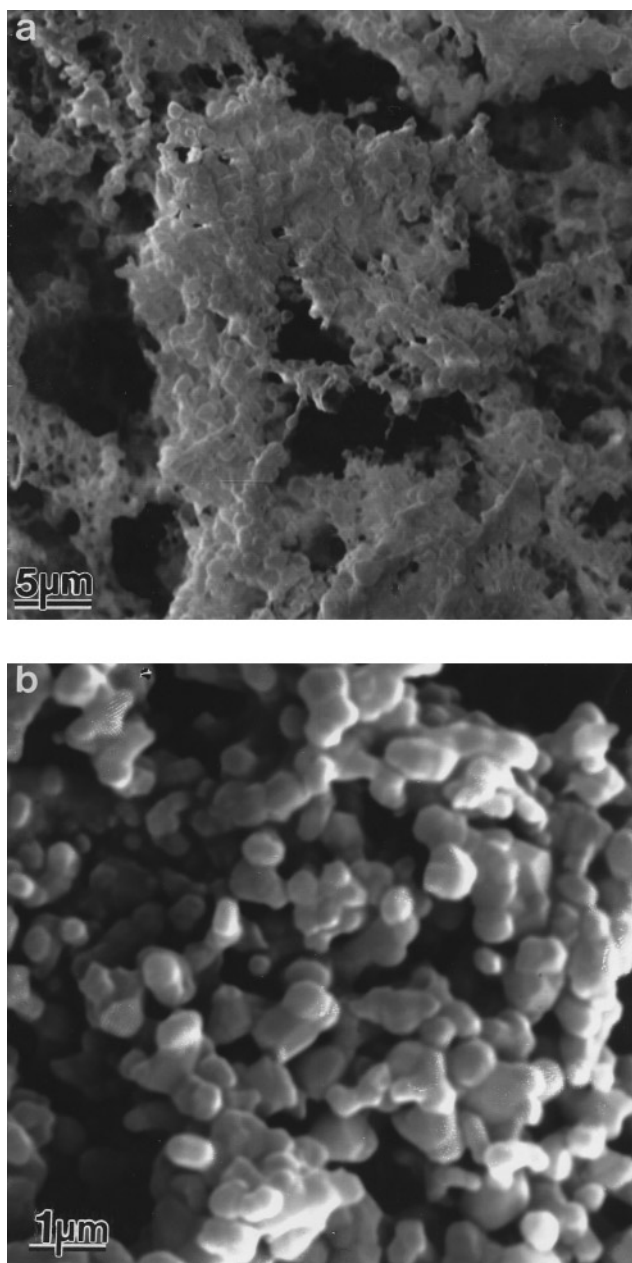
FIG. 2. SEM micrographs of LCM powders as synthesized (a) and after calcination (b).

TABLE 1
Atomic Ratio and Goldschmidt Tolerance Factor t for $La_{1-x}Ca_xMnO_3$ Powders with the Intended Composition (x)

x	$La_{1-x}Ca_xMnO_3$ $\mathrm{La:Ca:Mn:O}$	t
0.2	0.802 : 0.207 : 1 : 3.078	0.958
0.3	0.708 : 0.308 : 1 : 3.044	0.959
0.4	0.598 : 0.393 : 1 : 2.975	0.962
0.6	0.414 : 0.594 : 1 : 2.954	0.969

A homogeneous oxygen stoichiometry in the grains is important for the quality of the X-ray diffraction patterns.

The experimental X-ray powder pattern and difference between experimental spectrum and Rietveld profile fit are shown for $La_{0.8}Ca_{0.2}MnO_3$ in Fig. 3. The observed and calculated diffraction peaks of $La_{0.8}Ca_{0.2}MnO_3$ are given in Table 2.

Analysis of the full patterns and of individual reflections reveals that $La_{1-x}Ca_xMnO_3$ with $x = 0.2, 0.3, 0.4$, and 0.6 is orthorhombic at room temperature. The lattice parameters are related to the simple perovskite lattice parameter a_p by $a \approx c \approx \sqrt{2}a_p$ and $b \approx 2a_p$. For the X-ray data, the systematically absent reflections are consistent with the space group $Pnma$ (13–15). Our results fit in with those from a recent study on $La_{1-x}Ca_xMnO_3$, with two other doping levels ($x = 0.25$ and 0.5), by Radaelli *et al.* (5). The lattice parameters and the unit cell volume as a function of amount of calcium in LCM are plotted in Fig. 4a. The figure clearly demonstrates that the orthorhombic unit cell approaches a tetragonal cell as the amount of calcium increases. The unit cell volume decreases with increasing x. The ionic radii of the Ca^{2+} ion and the La^{3+} ion with a coordination number (CN) 12 are 1.35 and 1.32 Å, respectively (16). Although the radius of the Ca^{2+} ion is larger than that of the La^{3+} ion, both the cell parameters and the unit cell volume decrease with increasing x. The unit cell contraction is explained by the increase of the Mn^{4+} content which can be calculated directly from the results of the iodometric titration (7). The ionic radius of Mn^{4+} (0.54 Å) in an octahedral site is smaller than that of Mn^{3+} (0.65 Å) (16). The $Mn^{3+}/(Mn^{3+} + Mn^{4+})$ ratio and the oxygen nonstoichiometry as a function of amount of calcium in LCM is plotted in Fig. 4b.

In the orthorhombic unit cell, A site cations (La and Ca) coordinate with 12 anions: 4 O(1) and 8 O(2) ions. B site cations (Mn) coordinate with 6 anions: 2 O(1) and 4 O(2) ions. Refined lattice parameters and residuals R_{wp} from the Rietveld analysis program GSAS are listed in Table 3. In Table 4 the refined atomic positions are given. The consistency and reproducibility of the results was checked by comparing them with those obtained by the Rietveld analysis program WIN-RIETVELD. The results from the two
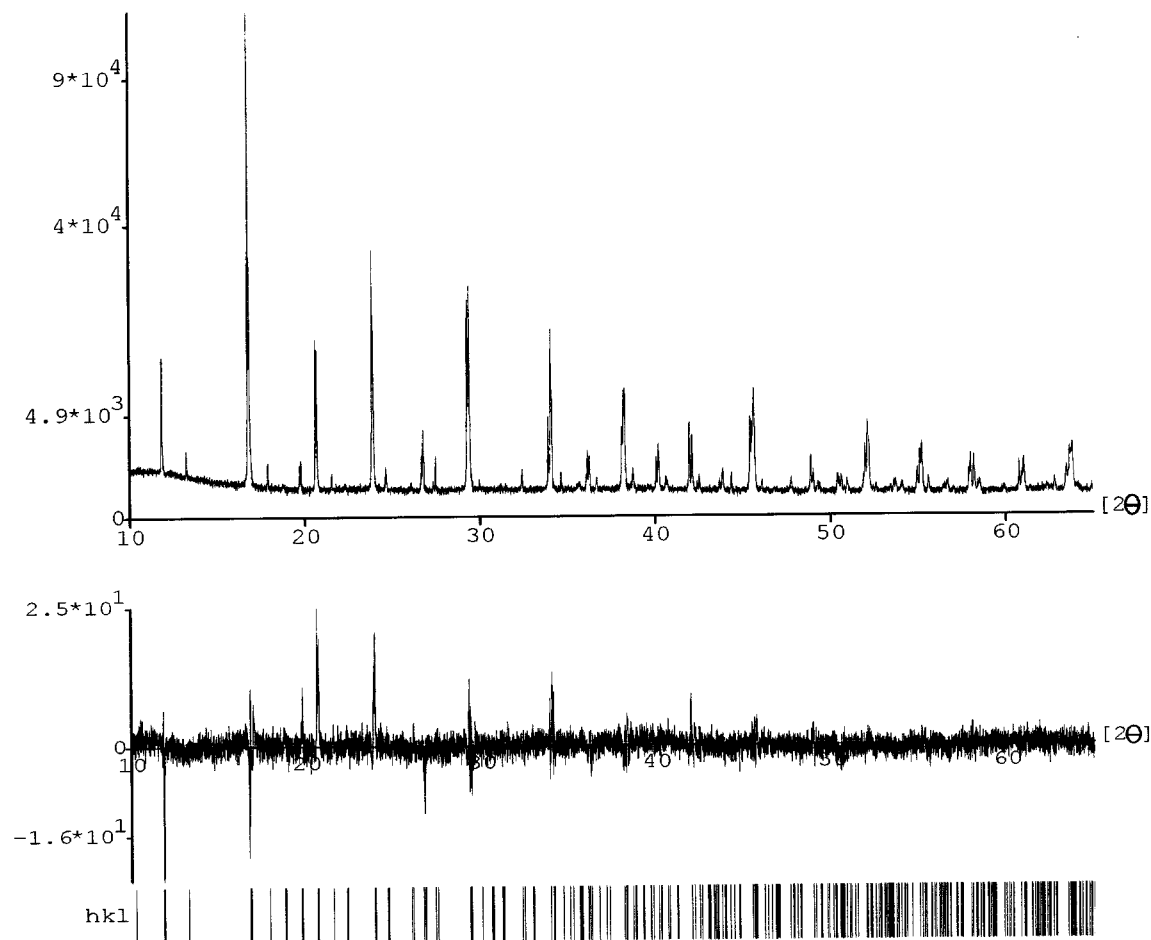
due to impurities are absent. The X-ray diagrams obtained for the different compositions were all much alike, except for the difference in line splittings. The degree of line splittings decreased with increasing amount of calcium in LCM. However, for a given composition there was a significant difference between "slow" and "fast" cooled powders. The full-width at half-maximum (FWHM) was reduced from 0.08 to 0.05° by the slower cooling rate, indicating better crystallinity and homogeneity of the samples.

FIG. 3. Experimental and difference X-ray powder patterns for $La_{0.8}Ca_{0.2}MnO_3$.

programs were consistent within the standard deviations but the R factors were higher and the refinement less stable with the WIN-RIETVELD program. Thus, bond lengths and angles were calculated using the coordinates from the GSAS program. R_{wp} is the weighted residual which is minimized in the least-squares algorithm. Therefore, R_{wp} is the most significant number in the refinement process. The final R_{wp} of all samples was less than 14%. This suggests that the structural model for $La_{1-x}Ca_xMnO_3$ is reasonable since R_{wp} is higher for synchrotron radiation than for monochromatic $CuK\alpha$ radiation due to difficulties in describing the profile function. But the R_{wp} values given for this structure are still rather high due to the fact that two of the lattice parameters are almost identical. In the present study isotropic thermal parameters (B) for the La, Ca, Mn, O(1), and O(2) ions were fixed at $0.4\,\text{Å}^2$ for all samples, nor were the population parameters refined. Our results are in good agreement with the results on $La_{1-x}Ca_xMnO_{2.97}$ $(0.9 < x < 1.0)$ by Taguchi [19].

Table 5 shows the Mn–O distances of $La_{1-x}Ca_xMnO_3$ calculated from the refined structure by using the EUTAX program [20]. The Mn–O (1 and 2) distances decrease with increasing x as a consequence of the increasing amount of Mn^{4+}. The O(1)–Mn–O(1) and O(2)–Mn–O(2) angles in $La_{1-x}Ca_xMnO_3$ were found to deviate no more than 0.01 from 180°, and the two different O(1)–Mn–O(2) angles listed in Table 6 deviate no more than 0.9 from 90°. Thus, the MnO_6 octahedra are fairly symmetrical for all the compositions like that in orthorhombic (ORT2) $LaMnO_{3.15}$ at 9 K studied by Hauback et al. [21]. However, Table 6 shows that the angles for Mn–O(1 and 2)–Mn are considerably less than 180°, indicating a tilting of the MnO_6 octahedra. The distorted perovskite structure of $La_{0.8}Ca_{0.2}MnO_3$ is illustrated in Fig. 5.

The Goldschmidt tolerance factor, t, is an important criterion for obtaining information on the distortion of the perovskite lattice and is given by $t = (R_A + R_B)/\sqrt{2(R_B + R_O)^2}$, where R_A, R_B, and R_O are the ionic radii of the A and B site cations and the oxygen anion, respectively, in ABO_3 perovskites. The Goldschmidt tolerance factor t for each composition given in Table 1 is calculated using the ionic radii given by Shannon and Prewitt [16]. For the

TABLE 2
Observed and Calculated X-Ray Diffraction Peaks for
Orthorhombic $La_{0.8}Ca_{0.2}MnO_3$

hkl	2θ (obs)	2θ (calc)	Difference
101	11.8425	11.8397	0.0028
020	11.8700	11.8722	−0.0022
111	13.2575	13.2555	0.0020
002	16.7466	16.7452	0.0014
121	16.8175	16.8149	0.0026
210	17.8720	17.8704	0.0016
112	19.7006	19.6995	0.0011
211	19.7595	19.7592	0.0003
022	20.5934	20.5936	−0.0002
220	20.6715	20.6699	0.0016
202	23.8519	23.8520	−0.0001
040	23.9189	23.9180	0.0009
212	24.6013	24.6027	−0.0014
103	26.6594	26.6619	−0.0025
222	26.7374	26.7367	0.0007
141	26.7773	26.7812	−0.0039
311	27.4555	27.4575	−0.0020
123	29.2876	29.2898	−0.0022
042	29.3650	29.3582	0.0068
240	29.4019	29.4131	−0.0112
331	32.4021	32.4007	0.0014
004	33.9023	33.9073	−0.0050
242	34.0506	34.0515	−0.0009
400	34.1000	34.0997	0.0003
410	34.6423	34.6457	−0.0034
143	36.1384	36.1378	0.0006
341	36.2364	36.2290	0.0074
204	38.1068	38.1035	0.0033
323	38.1825	38.1797	0.0028
161	38.2665	38.2662	0.0003
412	38.7285	38.7296	−0.0011

TABLE 3
Refined Lattice Parameters in Å for $La_{1-x}Ca_xMnO_3$ Calculated
by the Rietveld Analysis Program GSAS

x	R_{wp}	R_p	χ^2	a (Å)	b (Å)	c (Å)
0.2	12.25	9.01	2.15	5.4665(1)	7.7306(1)	5.4967(1)
0.3	10.42	7.45	3.36	5.4615(1)	7.7190(1)	5.4827(1)
0.4	13.84	10.43	1.89	5.4473(1)	7.6940(1)	5.4621(1)
0.6	11.91	9.11	3.27	5.4033(1)	7.6127(1)	5.4125(1)

ideal perovskite structure, t is unity. For $\sim 0.75 < t \leq 1.0$, however, the structure distorts to tetragonal, rhombohedral or as in the case of $La_{1-x}Ca_xMnO_3$, orthorhombic symmetry. As can be seen from Table 1, t increases with increasing x which implies that the orthorhombic unit cell approaches a tetragonal cell as the amount of calcium increases as stated previously.

IR spectra of $La_{0.8}Ca_{0.2}MnO_3$ and $La_{0.4}Ca_{0.6}MnO_3$ powders with different thermal histories are shown in Fig. 6a and b. The IR spectra of the raw powders show broad amorphous like absorption peaks in the whole frequency region. The powders have experienced temperatures above 1000°C during the combustion reaction (6). However, the temperature–time profile during the combustion is not controlled, and after ignition the powder is quenched to room temperature at a rate in the order of 100°C/s. The oxygen partial pressure during cooling might also deviate from ambient, and the oxygen nonstoichiometry of the raw powders might be different from the annealed powders. The broad IR absorption bands of the raw powders might therefore be due to inhomogeneous oxygen nonstoichiometry of
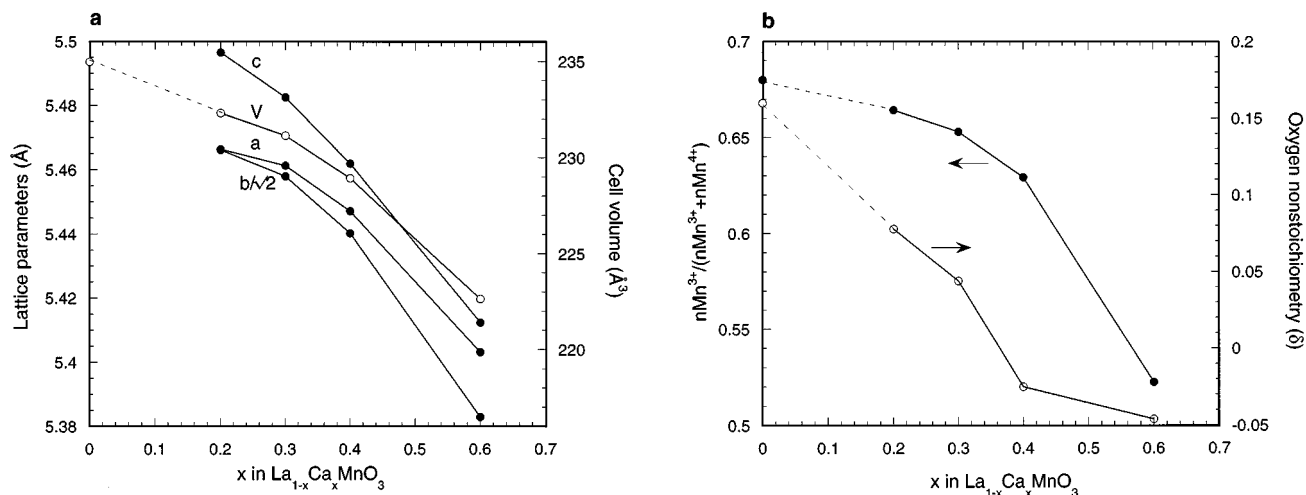

FIG. 4. (a) Lattice parameters and unit cell volume of $La_{1-x}Ca_xMnO_3$ as a function of x as obtained from high resolution synchrotron X-ray powder diffraction data. The unit cell volume for $x = 0$ has been calculated by multiplying the hexagonal volume (17) by 12/18 to obtain an "orthorhombic" cell. (b) $Mn^{3+}/(Mn^{3+} + Mn^{4+})$ ratio (filled circles) and oxygen nonstoichiometry, δ (open circles), as a function of x as obtained from iodometric titration. The error bars are smaller than the symbols. Lines through the points are guides for the eye. The $Mn^{3+}/(Mn^{3+} + Mn^{4+})$ ratio for $x = 0$ is calculated based on the oxygen stoichiometry for $LaMnO_{3.158}$ given by Van Roosmalen et $al.$ (18).

TABLE 4
Refined Atom Positions for $La_{1-x}Ca_xMnO_3$ Calculated by the Rietveld Analysis Program GSAS

x	Atom	Position	x	y	z
0.2	La, Ca	4(c)	0.01754(9)	0.25	−0.00306(9)
	Mn	4(b)	0	0	0.5
	O(1)	4(c)	0.4976(11)	0.25	0.0645(10)
	O(2)	8(d)	0.2738(12)	0.0327	−0.2696(12)
0.3	La, Ca	4(c)	0.01805(8)	0.25	−0.00325(8)
	Mn	4(b)	0	0	0.5
	O(1)	4(c)	0.4942(10)	0.25	0.0651(10)
	O(2)	8(d)	0.2773(10)	0.0319(5)	−0.2720(10)
0.4	La, Ca	4(c)	0.01833(15)	0.25	−0.00327(15)
	Mn	4(b)	0	0	0.5
	O(1)	4(c)	0.4962(15)	0.25	0.0624(18)
	O(2)	8(d)	0.2748(18)	0.0336(8)	−0.2778(16)
0.6	La, Ca	4(c)	0.01799(15)	0.25	−0.00271(15)
	Mn	4(b)	0	0	0.5
	O(1)	4(c)	0.4918(15)	0.25	0.0722(13)
	O(2)	8(d)	0.2737(16)	0.0318(6)	−0.2718(17)

TABLE 5
Mn–O(1) and the Two Different Mn–O(2) Distances of $La_{1-x}Ca_xMnO_3$

x	Mn–O(1) (Å)	Mn–O(2) (Å)	Mn–O(2) (Å)
0.2	1.965(1)	1.946(2)	1.977(3)
0.3	1.963(1)	1.940(3)	1.979(4)
0.4	1.954(1)	1.944(4)	1.968(3)
0.6	1.943(1)	1.928(3)	1.942(2)

the powders. In addition, A and B site disorder and the small crystallite size may also contribute to the broadening of the vibrational bands.

After annealing at 1000°C, the IR spectra of the powders showed more defined structures and significantly less peak broadening, especially at high La content as shown in Fig. 6a. The particle and crystallite size have increased during annealing as demonstrated in Fig. 2. Grain growth during annealing is also manifested by the reduced surface area and by the dramatically narrowed Bragg reflections. However, a significant difference in the spectra of powders was observed using "slow" (5 and 2°C/h, Fig. 1) and "fast" (25°C/h) cooling rates, especially for $La_{0.4}Ca_{0.6}MnO_3$ shown in Fig. 6b. The vibrational bands become sharper after the "slow" cooling. Correspondingly, the FWHM of Bragg reflections were also decreased by decreasing the cooling rate as argued previously. Due to the "fast" cooling rate, some kind of inhomogeneity or disorder must occur. The oxygen nonstoichiometry of $La_{1-x}Ca_xMnO_{3\pm\delta}$ is temperature dependent (22), but with decreasing temperature the oxidation
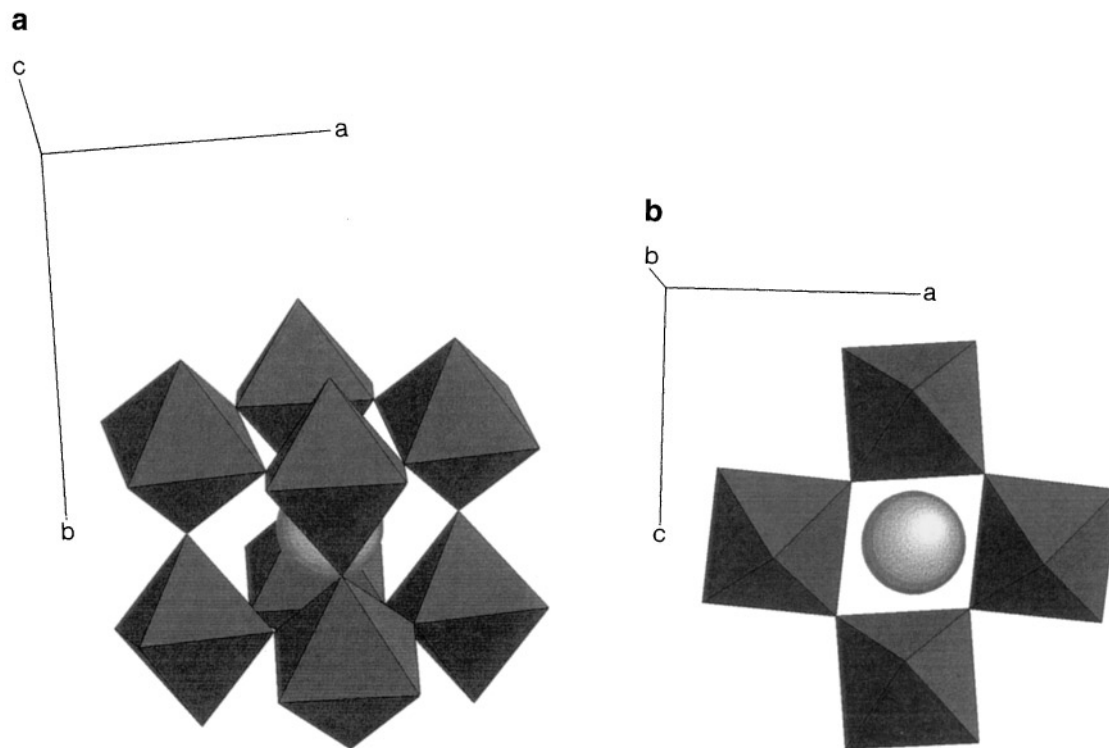

FIG. 5. Representation of the distorted perovskite structure of $La_{0.8}Ca_{0.2}MnO_3$. (a) Part of the crystal corresponding to the ideal, cubic perovskite unit cell. (b) The same part viewed parallel to the b axis. The atom in the middle is La.

TABLE 6
Mn–O–Mn and O–Mn–O Angles for La$_{1-x}$Ca$_x$MnO$_3$

x	Mn–O(1)–Mn (deg)	Mn–O(2)–Mn (deg)	O(1)–Mn–O(2) (deg)	O(1)–Mn–O(2) (deg)
0.2	159.2(6)	162.2(8)	90.3(5)	90.2(7)
0.3	159.0(7)	161.7(7)	90.2(6)	90.2(7)
0.4	159.9(9)	160.7(7)	90.7(6)	90.0(7)
0.6	156.6(7)	162.3(8)	91.3(5)	90.9(5)

rate decreases. At a given temperature the oxygen nonstoichiometry becomes apparently temperature independent. One might speculate whether this reflects the thermodynamics or whether this is governed by slow kinetics of the oxidation of the material during cooling. Since the cooling rate effects the properties of the powders, the kinetics of the oxidation are the most probable reason for the inhomogeneity. The diffusion of oxygen is probably the limiting factor, and we therefore suggest that the broadening of the "fast"

cooled samples is due to inhomogeneous oxygen stoichiometry.

IR spectra of "slow" cooled powders are shown as function of Ca content in Fig. 6c. The spectra are in relatively good agreement with recently published spectra reported for La$_{1-x}$Ca$_x$MnO$_3$, $x = 0.3$ (23) and 0.175 (24). The spectra can be interpreted in terms of the three triple degenerate IR-active vibrational modes of the ideal cubic perovskite structure: B–O stretching mode, O–B–O bending mode, and A site external mode in the descendant order of frequency. The absorption peaks at around 600, 400, and 200 cm^{-1} can therefore be assigned to Mn–O stretching, O–Mn–O bending mode, and motion of La or Ca cations relative to the MnO$_6$ octahedra.

Since the symmetry of La$_{1-x}$Ca$_x$MnO$_3$ is less than cubic, a splitting of the degenerate IR modes are expected. An orthorhombic distortion from cubic will result in a splitting into three nondegenerate modes. The splitting of the IR active modes is expected to decrease with increasing content of Ca since the deviation from cubic structure is less significant. However, we do observe a more pronounced
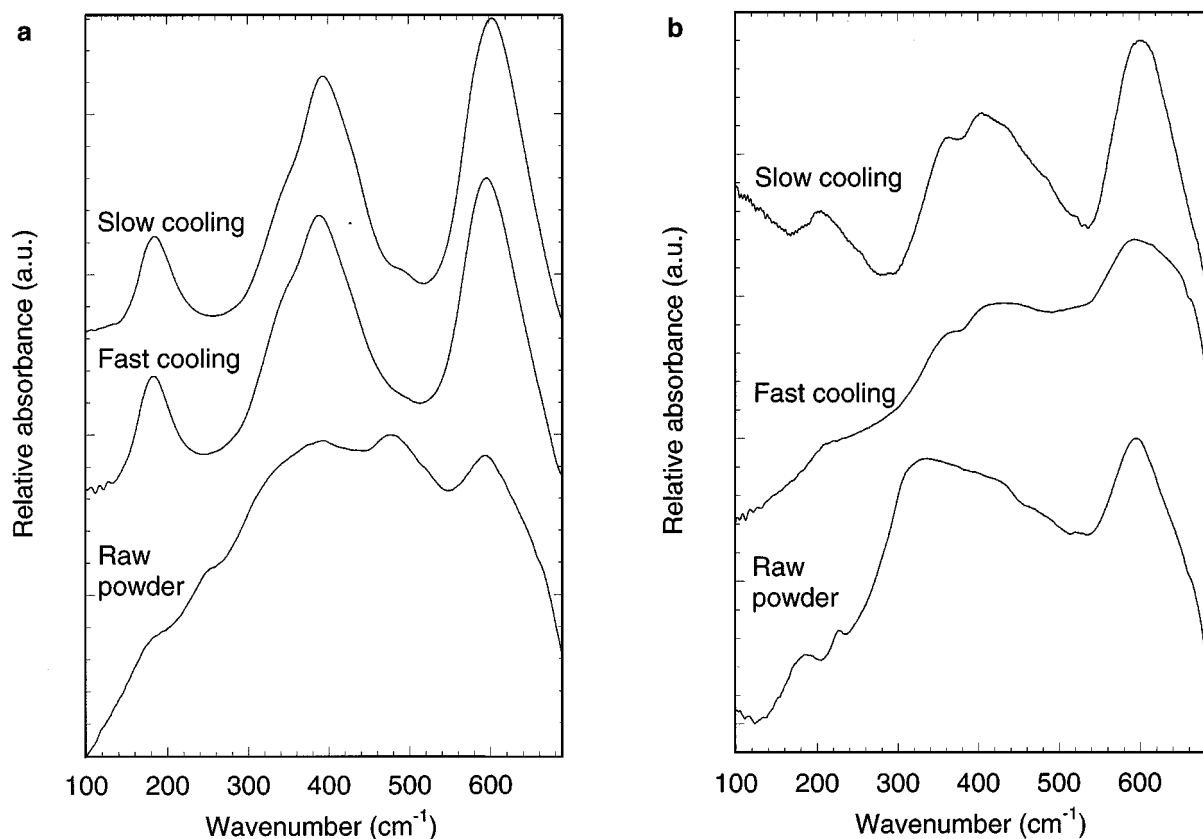

FIG. 6. IR spectra of raw powders, "slow" and "fast" cooled powders of (a) La$_{0.8}$Ca$_{0.2}$MnO$_3$ and (b) La$_{0.4}$Ca$_{0.6}$MnO$_3$ and (c) "slow" cooled powders of La$_{1-x}$Ca$_x$MnO$_3$, $x = 0.2$, 0.3, 0.4, and 0.6.
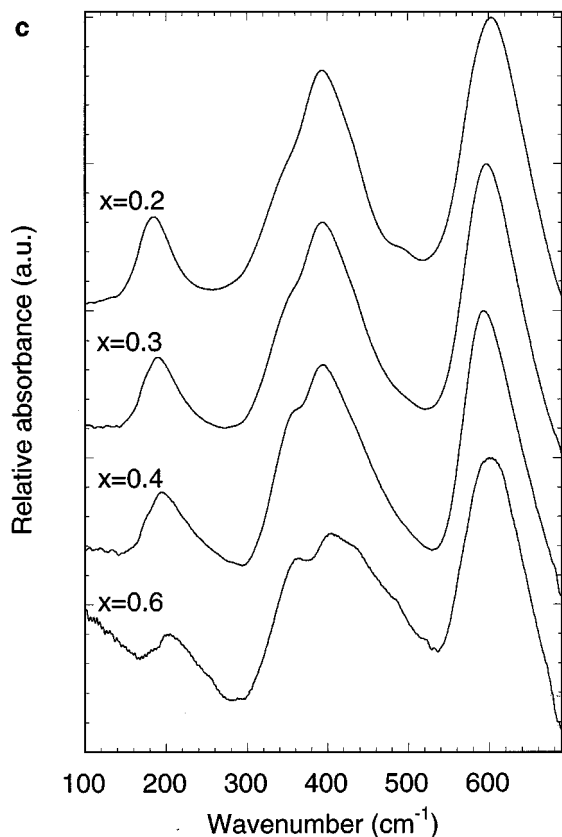
FIG. 6—Continued

splitting/broadening of the O–Mn–O bending mode as the Ca content increases. We propose that the new bands appearing are due to an effect of substituting Ca for La and

hence a change in mass of the A site cation. This proposal is supported by the fact that the O–Mn–O bending is shifted to slightly higher frequency with increasing Ca content. No significant broadening of the Mn–O stretching mode could be observed as the Ca content was increased; however, we expect the O–Mn–O bending mode to be the most dependent on the presence of La or Ca.

The frequency of the La(Ca)–O external mode at about $200 \, cm^{-1}$ is increasing with increasing Ca content. This frequency shift is expected based on the lower mass of Ca relative to La. Assuming a harmonic oscillator and the same A–O force constant, the frequency would increase from $180 \, cm^{-1}$ for La to $201 \, cm^{-1}$ for Ca. The observed trend fits nicely with these calculations even considering a small increase in the force constant exchanging Ca for La. A broadening of this band is also observed as the Ca content is increasing. The formal oxidation state of Mn does not appear to have a significant contribution to the vibrational density of states.

The space group $Pnma$ determined by high resolution synchrotron X-ray powder diffraction has point group mmm. Electron diffraction (SAED and CBED) was performed to verify the point group symmetry. Figure 7 shows two different portions of the CBED pattern: the whole pattern (WP) and its corresponding zero-order Laue zone (ZOLZ) pattern. This orientation was recognized as (010). The bright-field (BF) pattern from the (000) spot of $La_{1-x}Ca_xMnO_3$ is not included because the higher-order Laue zones (HOLZ) lines from high-symmetry zone axes in orthorhombic $La_{1-x}Ca_xMnO_3$ at room temperature are diffuse and weak due to thermal damping and absorption. The WP and projection diffraction symmetries (PDS) are both $2mm$. Thus, with a reference to the tables of Buxton
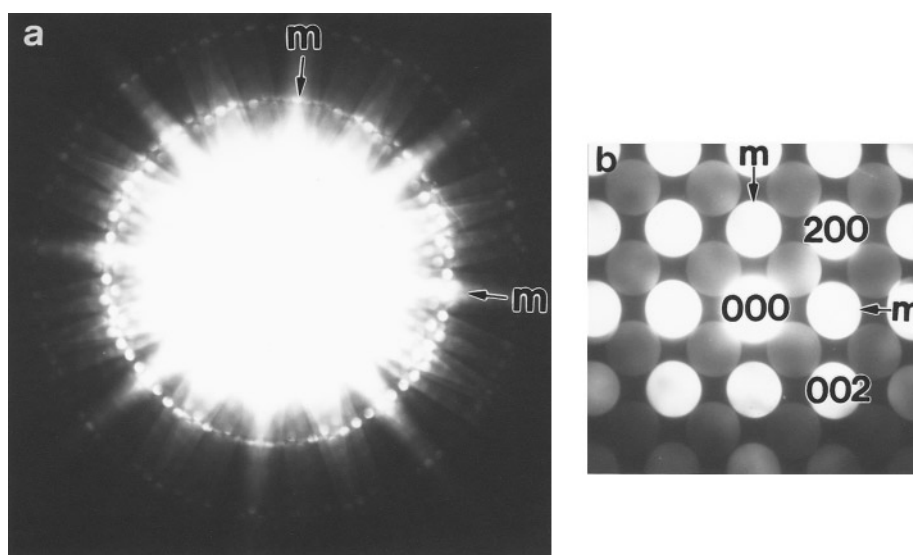
FIG. 7. [010] zone axis pattern from $La_{0.8}Ca_{0.2}MnO_3$. (a) WP and (b) ZOLZ pattern.

et al. (25), the crystal posesses diffraction group $2mm1_R$, $2mm$, or $4_R mm_R$. Two other high-symmetry CBED patterns, similar to the one above, (recognized as (100) and (001)), also exhibited the same diffraction groups. Furthermore, no other zone axis with symmetries higher than $2mm$ could be found. This fact rules out the $4_R mm_R$ diffraction group as a possibility. Defining the unit-cell axes along the three orthogonal directions, the above observations confirm the Bravais lattice of $La_{1-x}Ca_x MnO_3$ to be orthorhombic since only orthorhombic crystals have $2mm$ symmetry in three mutually orthogonal directions. In orthorhombic crystals, only crystals of the *mmm* point group show $2mm1_R/2mm$ diffraction groups in three different zone axes (25). Further, other zone axes also showed symmetries expected from the *mmm* point group as summarized in Table 7. Since the *mmm* point group consists of only twofold screw/rotation axes and (100), (010), and (001) glide planes, $\langle uv0 \rangle$, $\langle u0w \rangle$, and $\langle 0vw \rangle$ type zone axes are appropriate for investigation as the BF and WP symmetries of these axes correspond to a single mirror "m" (25). Figure 9 shows the $(01\bar{2})$ zone axis CBED and SAED patterns from $La_{0.8}Ca_{0.2}MnO_3$. The WP symmetry is "m". Thus with reference to Table 7, the point group of $La_{1-x}Ca_x MnO_3$ is established as *mmm*.

The unit cell type of orthorhombic $La_{1-x}Ca_x MnO_3$ was readily determined by overlaying the first-order Laue zone (FOLZ) reflections onto the ZOLZ reflections for all of the three $\langle 010 \rangle$ type zone axes. When this was done, the FOLZ reflections superimposed onto the ZOLZ, indicating that the unit cell in reciprocal space is primitive. Thus, the real-space unit cell will also be primitive.

Having determined the room-temperature crystal form of $La_{1-x}Ca_x MnO_3$ to be orthorhombic and primitive, we are able to generate the orthorhombic cell from the simple cubic perovskite cell as shown in Fig. 8, which is the (010) projection of four orthorhombic cells. One can envisage the creation of the orthorhombic cell from the simple cubic
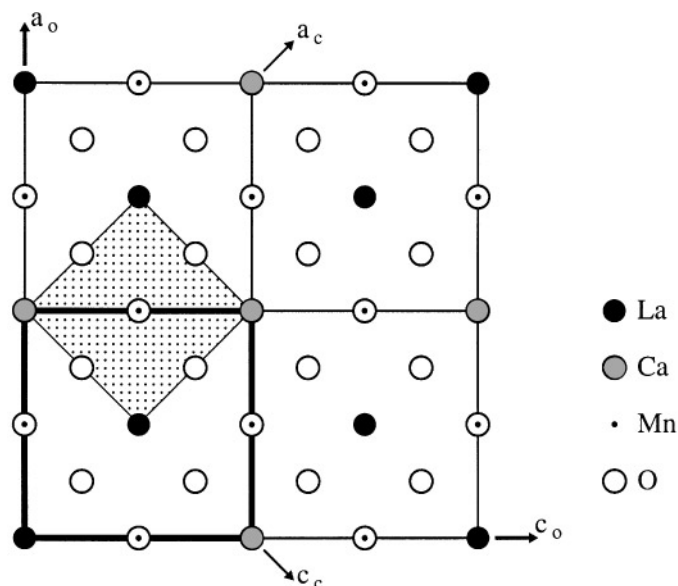

FIG. 8. (010) projection of four orthorhombic unit cells of $La_{1-x}Ca_x MnO_3$. Lattice correspondence between the simple cubic unit cell (shaded square) and the orthorhombic cell (thick outline) is indicated. The $\vec{b}$ axis of the orthorhombic cell is double the $\vec{b}$ axis of the simple cubic cell, which is normal to the plane of the paper.

perovskite cell by the matrix transformation:

$$\begin{pmatrix} a_0 \\ b_0 \\ c_0 \end{pmatrix} = \begin{pmatrix} 1 & 0 & \bar{1} \\ 0 & 2 & 0 \\ 1 & 0 & 1 \end{pmatrix} \begin{pmatrix} a_c \\ b_c \\ c_c \end{pmatrix},$$

where a_0, b_0, and c_0 are the unit cell vectors of the orthorhombic cell and a_c, b_c, and c_c are the unit cell vectors of the simple cubic unit cell.

In $La_{0.8}Ca_{0.2}MnO_3$ we found diffraction evidence of a superstructure in domains in some of the grains. A $[10\bar{1}]$ zone axis electron diffraction pattern from two domains of the same grain indexed with the orthorhombic crystal structure determined is represented in Fig. 10 a and b. Figure 10c shows the grain lying on a holey carbon net. In Fig. 10b sharp superlattice spots are evident in addition to the fundamental Bragg reflections. The detection of superlattice spots provides structural evidence of cation ordering. The presence of superlattice spots with modulation wave vector $(\frac{1}{2} v \frac{1}{2})$ are evident, indicating a $2a \times b \times 2c$ supercell. The kinematically forbidden (010) spot also appears as a result of multiple scattering in zero-order Laue zone (ZOLZ) $(010 = 111 + \bar{1}0\bar{1})$. We assume that the superstructure in $La_{0.8}Ca_{0.2}MnO_3$ is due to ordering of Ca^{2+} ions on A (La^{3+}) sites in the perovskite ABO_3 structure. Figure 8 shows a (010) projection of four orthorhombic cells building up the supercell. The $\vec{a}$ and $\vec{c}$ axes of the supercell are double the $\vec{a}$ and $\vec{c}$ axes of the orthorhombic cell due to Ca^{2+} on

TABLE 7
Whole Pattern Symmetries and Corresponding Diffraction Groups in $La_{1-x}Ca_x MnO_3$

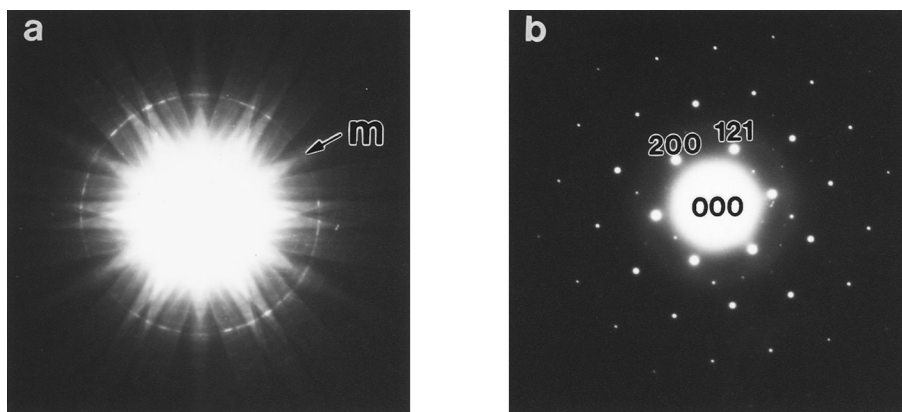| Zone axis	Whole pattern projection symmetry	Whole pattern symmetry	Deduced diffraction groups
[100]	$2mm$	$2mm$	$2mm1_R/2mm$
[010]	$2mm$	$2mm$	$2mm1_R/2mm$
[001]	$2mm$	$2mm$	$2mm1_R/2mm$
[101]	$2mm$	m	$2_R mm_R$
[011]	$2mm$	m	$2_R mm_R$
$[01\bar{2}]$		m	$2_R mm_R/m/m1_R$

FIG. 9. $[01\bar{2}]$ zone axis pattern from $La_{0.8}Ca_{0.2}MnO_3$. (a) CBED WP symmetry and (b) SAED. The diffuse rings come from the carbon net that supports the powder.

every second La^{3+} site. This cation configuration gives a Ca to La ratio of $3/13 \sim 0.231$ which is close to the original Ca to La ratio of 0.258 in $La_{0.8}Ca_{0.2}MnO_3$. The $2a \times b \times 2c$ supercell is analogous to the supercell suggested from previous transport and magnetic susceptibility measurements on $La_{0.5}Ca_{0.5}MnO_3$ at low temperatures, where a $2a \times b \times 2c$ supercell was found to be due to charge ordering (5, 26).

4. CONCLUSIONS

$La_{1-x}Ca_xMnO_{3\pm\delta}$ powders with $x = 0.2, 0.3, 0.4,$ and 0.6 produced by the glycine/nitrate method, have a BET specific area of about 5.5 m^2/g after ball-milling, calcination, and further ball-milling. To prepare a high quality powder with a homogeneous oxygen stoichiometry a "slow" cooling rate (2–5°C/h) is necessary. The samples with $x = 0.2$ and 0.3 are cation deficient, while the samples with $x = 0.4$ and 0.6 are anion deficient relative to the ideal perovskite stoichio-

metry. The structure analyses reveal that $La_{1-x}Ca_xMnO_3$ with $x = 0.2, 0.3, 0.4,$ and 0.6 has orthorhombic symmetry with space group *Pnma*. The orthorhombic unit cell approaches a tetragonal cell as the amount of calcium increases. The unit cell volume decreases with increasing amount of calcium due to the increasing amount of Mn^{4+}. The MnO_6 octahedra are fairly symmetrical. However, the octahedra are tilted about 20° relative to the ideal perovskite structure. Infrared spectroscopy revealed that only the O–Mn–O bending mode is significantly influenced by the substitution of La with Ca.

In $La_{0.8}Ca_{0.2}MnO_3$ we found diffraction evidence of a superstructure. We assume that the superstructure in $La_{0.8}Ca_{0.2}MnO_3$ is due to ordering of Ca^{2+} ions on A (La^{3+}) sites in the perovskite ABO_3 structure. The $\vec{a}$ and $\vec{c}$ axes of the supercell are double the $\vec{a}$ and $\vec{c}$ axes of the orthorhombic cell due to Ca^{2+} on every second La^{3+} site.
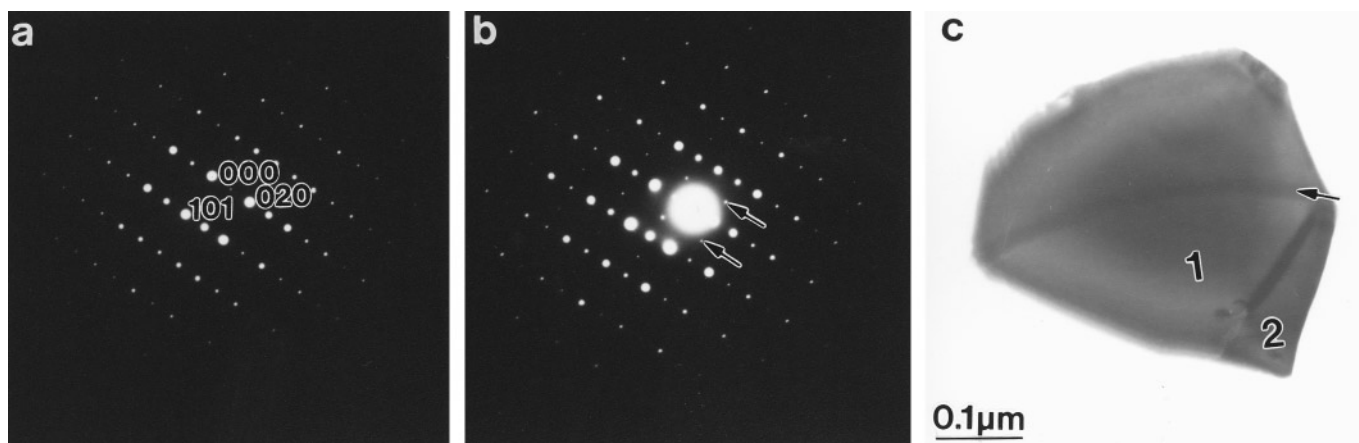

FIG. 10. $[10\bar{1}]$ zone axis pattern from two different domains of the same grain of $La_{0.8}Ca_{0.2}MnO_3$. In (a) no superstructure is seen, but in (b) which is taken from domain 2, sharp superlattice spots marked by arrows are evident. In (c) is shown the grain with the two domains, 1 and 2, lying on a holey carbon net. The contrast marked by an arrow is due to the carbon net.

REFERENCES

1. H. Taimatsu, K. Wada, H. Kaneko, and H. Yamamura, *J. Am. Ceram. Soc.* **75**(2), 401–405 (1992).
2. J. A. Brug, T. Anthony, and J. H. Nickel, *MRS Bull.* **21**(Sept.), 23–27 (1996).
3. P. Shuk, L. Tichonova, and U. Guth, *Solid State Ionics* **68,** 177–184 (1994).
4. R. Mahendiran, S. K. Tiwary, A. K. Raychaudhuri, T. V. Ramakrishnan, R. Mahesh, N. Rangavittal, and N. R. Rao, *Phys. Rev. B* **53**(6), 3348–3358 (1996).
5. P. G. Radaelli, D. E. Cox, M. Marezio, S.-W. Cheong, P. E. Schiffer, and A. P. Ramirez, *Phys. Rev. Lett.* **75**(24), 4488–4491 (1995).
6. L. A. Chick, L. R. Pederson, G. D. Maupin, J. L. Bates, and L. E. Thomas, *Mater. Lett.* **10**(6) (1990).
7. G. H. Jonker and J. H. van Santen, *Physica XVI*(3), 337–349 (1950).
8. D. Alexander, "PEAKFIND." ICI, England, 1973.
9. J. W. Visser, *J. Appl. Crystallogr.* **2,** 89–95 (1969).
10. H. M. Rietveld, *J. Appl. Crystallogr.* **2,** 65–71 (1969).
11. A. C. Larson and R. B. Von Dreele, Report LA-UR-86-784, Los Alamos National Laboratory, Los Alamos, NM, 1987.
12. J. W. Stevenson, P. F. Hallmann, T. R. Armstrong, and L. A. Chick, *J. Am. Ceram. Soc.* **78**(3), 507–512 (1995).
13. M. A. Gilleo, *Acta Crystallogr.* **10,** 161 (1957).
14. J. B. A. A. Elemans, B. van Laar, K. R. van der Veen, and B. O. Loopstra, *J. Solid State Chem.* **3,** 238 (1971).
15. P. Norby, I. G. Krogh Andersen, and E. Krogh Andersen, *J. Solid State Chem.* **119,** 191 (1995).
16. R. D. Shannon and C. T. Prewitt, *Acta Crystallogr.*, *Sect. B* **25,** 925 (1968).
17. I. G. Krogh Andersen, E. Krogh Andersen, P. Norby, and E. Skou, *J. Solid State Chem.* **113,** 320–326 (1994).
18. J. A. M. Van Roosmalen, E. H. P. Cordfunke, R. B. Helmholdt, and H. W. Zandbergen, *J. Solid State Chem.* **110,** 100–105 (1994).
19. H. Taguchi, *J. Solid State Chem.* **124,** 360–365 (1996).
20. N. E. Brese and M. O'Keeffe, *Acta Crystallogr.*, *Sect. B* **47,** 192–197 (1991).
21. B. C. Hauback, H. Fjellvåg, and N. Sakai, *J. Solid State Chem.* **124,** 43–51 (1996).
22. J. A. M. van Roosmalen and E. H. P. Cordfunke, *J. Solid State Chem.* **110,** 109–112 (1994).
23. K. H. Kim, J. Y. Gu, H. S. Choi, G. W. Park, and T. W. Hoh, *Phys. Rev. Lett.* **77,** 1877–1880 (1996).
24. Y. Okimoto, T. Katsufuji, T. Urushibara, T. Arima, and Y. Tokura, *Phys. Rev. Lett.* **75,** 109–112 (1995).
25. D. F. Buxton, J. A. Eades, J. W. Steeds, and G. M. Rackham, *Philos. Trans. R. Soc. London, Ser. A* **281,** 171–194 (1976).
26. C. H. Chen and S.-W. Cheong, *Phys. Rev. Lett.* **76**(21), 4042–4045 (1996).